Wideband Self-Grounded Bow-Tie Antenna for Thermal MR

Received: 22 July 2019 | Revised: 7 January 2020 | Accepted: 27 January 2020

DOI: 10.1002/nbm.4274

RESEARCH ARTICLE

NMR IN BIOMEDICINE WILEY

Wideband Self-Grounded Bow-Tie Antenna for Thermal MR

Thomas Wilhelm Eigentler[1,2] | Lukas Winter[1,3] | Haopeng Han[1,4] | Eva Oberacker[1] | Andre Kuehne[5] | Helmar Waiczies[5] | Sebastian Schmitter[3] | Laura Boehmert[1,6] | Christian Prinz[1,6] | Hana Dobsicek Trefna[7] | Thoralf Niendorf[1,5,8]

[1]Berlin Ultrahigh Field Facility (B.U.F.F.), Max-Delbrück-Center for Molecular Medicine in the Helmholtz Association, Berlin, Germany

[2]Technische Universität Berlin, Chair of Medical Engineering, Berlin, Germany

[3]Physikalisch-Technische Bundesanstalt (PTB), Braunschweig und Berlin, Berlin, Germany

[4]Institute of Computer Science, Humboldt-Universitätzu Berlin, Berlin, Germany

[5]MRI.TOOLS GmbH, Berlin, Germany

[6]Charité - Universitätsmedizin Berlin, corporate member of Freie Universität Berlin, Humboldt-Universität zu Berlin, and Berlin Institute of Health (BIH), Berlin, Germany

[7]Department of Electrical Engineering, Chalmers University of Technology, Gothenburg, Sweden

[8]Experimental and Clinical Research Center (ECRC), a joint cooperation between the Charité Medical Faculty and the Max-Delbrück-Center for Molecular Medicine in the Helmholtz Association, Berlin, Germany

Correspondence
Thoralf Niendorf, PhD, Max Delbrueck Center for Molecular Medicine in the Helmholtz Association, Robert Roessle Strasse 10, 13125 Berlin, Germany.
Email: thoralf.niendorf@mdc-berlin.de

Funding information
Bundesministerium für Bildung und Forschung, Grant/Award Number: FKZ 13GW0102A, FKZ 13GW0102B; H2020 European Research Council, Grant/Award Number: 743077

Abstract

The objective of this study was the design, implementation, evaluation and application of a compact wideband self-grounded bow-tie (SGBT) radiofrequency (RF) antenna building block that supports anatomical proton (^{1}H) MRI, fluorine (^{19}F) MRI, MR thermometry and broadband thermal intervention integrated in a whole-body 7.0 T system.

Design considerations and optimizations were conducted with numerical electromagnetic field (EMF) simulations to facilitate a broadband thermal intervention frequency of the RF antenna building block. RF transmission (B_1^+) field efficiency and specific absorption rate (SAR) were obtained in a phantom, and the thigh of human voxel models (Ella, Duke) for ^{1}H and ^{19}F MRI at 7.0 T. B_1^+ efficiency simulations were validated with actual flip-angle imaging measurements. The feasibility of thermal intervention was examined by temperature simulations (f = 300, 400 and 500 MHz) in a phantom. The RF heating intervention (P_{in} = 100 W, t = 120 seconds) was validated experimentally using the proton resonance shift method and fiberoptic probes for temperature monitoring. The applicability of the SGBT RF antenna building block for in vivo ^{1}H and ^{19}F MRI was demonstrated for the thigh and forearm of a healthy volunteer.

The SGBT RF antenna building block facilitated ^{19}F and ^{1}H MRI at 7.0 T as well as broadband thermal intervention (234-561 MHz). For the thigh of the human voxel models, a B_1^+ efficiency ≥11.8 μT/√kW was achieved at a depth of 50 mm. Temperature simulations and heating experiments in a phantom demonstrated a temperature increase ΔT >7 K at a depth of 10 mm.

The compact SGBT antenna building block provides technology for the design of integrated high-density RF applicators and for the study of the role of temperature in

Abbreviations used: ^{1}H, proton; ^{19}F, fluorine; AFI, actual flip-angle imaging; B_1^+, transmit radio frequency field; EM, electromagnetic; EMF, electromagnetic field; ε_r, relative dielectric constant; FR4, flame-retardant substrate (class 4); MR thermometry, magnetic resonance thermometry; PFCE, perfluoro-15-crown-ether; PRFS, proton resonance frequency shift; PTFE, polytetrafluoroethylene; RF, radiofrequency; RFPA, radiofrequency power amplifier; SAR, specific absorption rate; SAR_{10g}, specific absorption rate averaged over 10 g material or tissue; S_{ij}, scattering matrix entry i,j; SGBT, self-grounded bow-tie; Thermal MR, thermal magnetic resonance; UHF-MR, ultrahigh field magnetic resonance.

(patho-) physiological processes by adding a thermal intervention dimension to an MRI device (Thermal MR).

KEYWORDS

broadband antenna, magnetic resonance, radiofrequency antenna, self-grounded bow-tie, thermal intervention, thermal magnetic resonance, ultrahigh field MR

1 | INTRODUCTION

Temperature is a critical attribute of life, since biological processes are highly sensitive to temperature changes. The aberrant thermal properties of pathological tissues have led to a strong interest in temperature as a clinical parameter, but this interest has been hampered by the lack of non-invasive methods to measure and manipulate temperature.[1-5] Vigorous efforts in fundamental research and (bio)engineering of electromagnetic (EM)-induced heating has resulted in an enormous body of literature, paving the way for further technical developments.[6-8]

Targeted radiofrequency (RF)-induced thermal intervention based on constructive interference of EM waves transmitted within an MRI system is conceptually appealing for pursuing image-guided mild hyperthermia and other thermal interventions including controlled release of therapeutics from nanocarriers that bestow environmental responsiveness to physiologically relevant changes in temperature.[6,9] The efficacy and release profiles of MR-sensitive fluorine payloads from thermos-responsive nanocarriers can be monitored and quantified with ^{19}F MRI, which could provide an ideal means to monitor the release kinetics and bioavailability of an MR visible cargo in vivo, which would be a major leap forward to temperature-induced drug delivery in vivo.[10] In vivo thermometry and thermal dose management are essential for temperature-triggered interventions or drug delivery, and are at the forefront of the awareness and attention of the corresponding research communities. Similar to proton, the fluorine resonance frequency is also affected by temperature and can be exploited for temperature monitoring of fluorinated probes.[11]

Ensuring a patient- and problem-oriented adaptation of the size, uniformity and location of the RF energy deposition in the target region is highly relevant for the thermal intervention, with the focal point quality being governed by the radiation pattern of the single RF transmit element, the RF channel count and the thermal intervention radiofrequency of the RF applicator.[12-15] Reports on the radiation pattern of resonant structures underline the benefits of dipole antenna arrays for enhancing the focal point quality in thermal interventions.[16] These pioneering developments include dipole configurations with a reduced size, using high-permittivity dielectric and low-loss materials for antenna shortening en route to high-density arrays.[17,18] The thermal intervention frequency is a significant parameter that impacts the focal point quality. While long RF wavelengths in tissue at 64 MHz (1.5 T) are not suitable to focus EM energy within small targeted areas, the shortened wavelength in tissue at ≥297 MHz (7.0 T) enables stronger focusing of RF fields, thanks to more localized interference patterns.[14,18] Theoretical research and numerical simulations of targeted RF heating have shown how an ultrahigh field MR (UHF-MR) instrument can be adapted to generate highly focused heat in regions of tissue by the use of RF antenna arrays.[18] Studies on ultimate intrinsic specific absorption rate (SAR) and RF applicator concepts suggested high frequencies of up to 1 GHz for a highly focused EM energy deposition.[12,13] Antenna count and positioning also influence the focal point quality.[13] Increasing the number of antennas enables a lower surface RF energy deposition, while the focal point quality can be improved by longitudinal steering using multiple rings of antenna along the z-dimension.[13,19] A variable frequency increases the degrees of freedom (amplitude, phase and frequency) to modulate the focal point quality.[13,19,20] Reports on this subject suggest an ideal intervention frequency or a mix of intervention frequencies for a particular target and target location.[19-23] A compact wideband antenna setup based on a self-grounded bow-tie (SGBT) antenna is a potential answer to the need for multiple rings and a high channel count setup to enable broadband thermal intervention.[19,22-24] While several previous reports on RF antenna systems have addressed these multiple issues individually,[8,15,18-20,25] our objective with this new design was to achieve a comprehensive solution.

Recognizing the opportunities of adding a thermal intervention dimension to an MRI device (Thermal MR) for studying the role of temperature in biological systems and disease, this work reports on the design process, implementation, evaluation and application of a compact wideband SGBT building block. We demonstrate the suitability of this design for thermal intervention, proton (^{1}H) MRI, ^{1}H MR temperature mapping and fluorine (^{19}F) MRI in a single device, integrated in a whole-body 7.0 T MRI system.

2 | METHODS

2.1 | RF antenna building block design considerations

The RF antenna building block consists of an SGBT antenna with a dielectric material filled housing (Figure 1A). The SGBT antenna is based on a design with a strong main lobe directivity and limited back radiation due to the self-grounded backplane.[24] This feature makes it an ideal

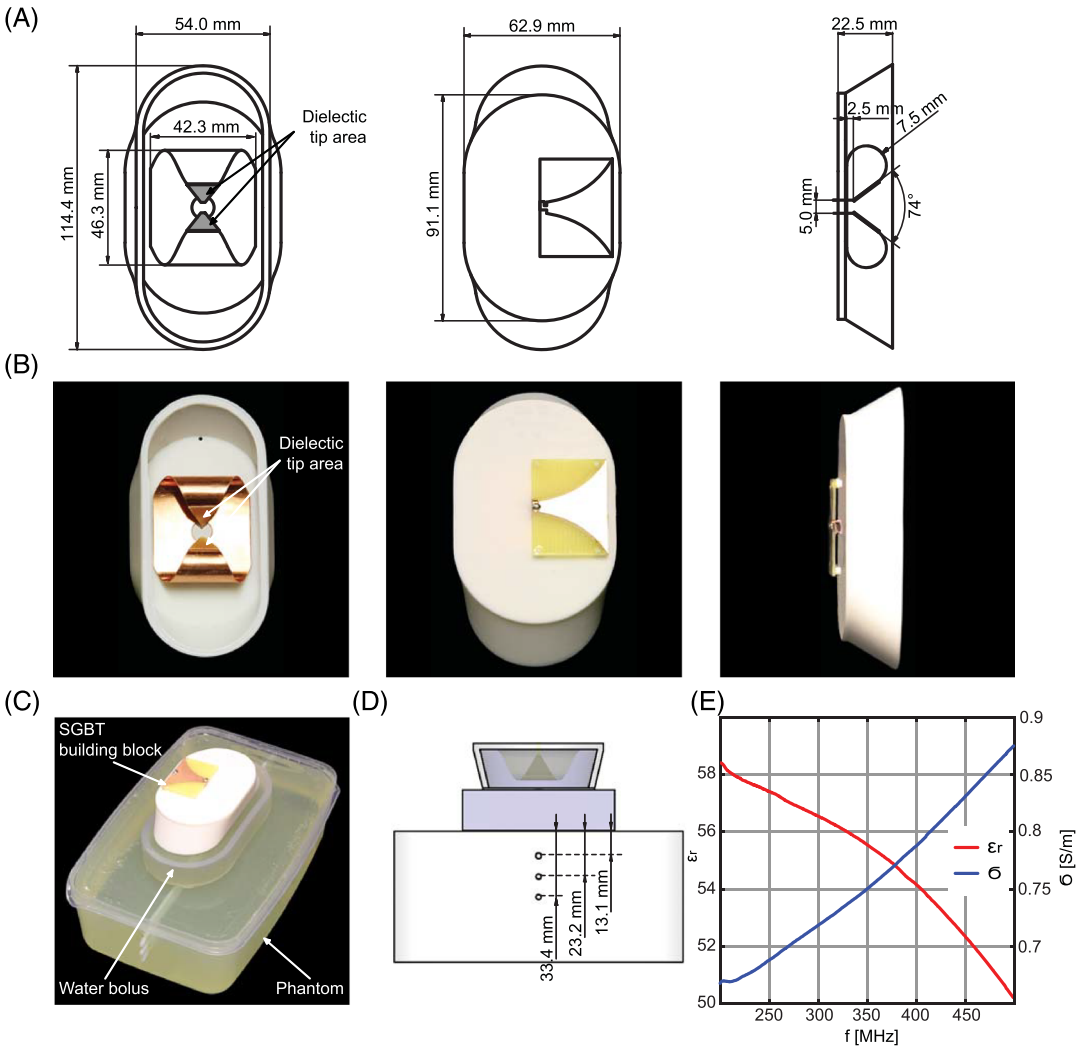

FIGURE 1 (A) Basic scheme of the SGBT building block, balun and SGBT antenna design. (B) Additively manufactured building block with the SGBT antenna placed inside the housing and with the balun positioned on top of the building block. (C) Experimental setup with SGBT building block, water bolus and phantom used for magnetic transmission field assessment and thermometry measurements. (D) Basic scheme of the setup including the positioning of small tubes within the phantom (length = 210 mm; width = 140 mm; depth = 64 mm) for accommodating fiberoptic probes for temperature measurements or a fluorinated compound for fluorine MRI. (E) Measured broadband material characteristics of the used phantom for a frequency ranging from 200 to 500 MHz

candidate for a highly efficient thermal intervention antenna with the ability of MR imaging at 7.0 T.[22,23] A deuterium oxide (D_2O, 99.9%, $\varepsilon_r \approx 81$ at 297.2 MHz, Sigma Aldrich GmbH, Munich, Germany) filled housing was used to shorten the effective transmit RF wavelength to reduce the overall antenna size.[17-19]

The SGBT antenna was manufactured with 0.3 mm copper, to guarantee a mechanically robust antenna system. A low-permittivity dielectric material was used to improve the broadband characteristics by spreading the electric field in the tip area of the antenna.[19] The dielectric material thickness was found to have a minor influence on the broadband characteristics, so that 0.5 mm FR4 was used to limit the degrees of freedom for the antenna optimization. Additive manufacturing based on lithography (Form2, Formlabs, Somerville, MA) was used to model the housing of the building block (Figure 1B). A balanced to unbalanced (balun) transformer, manufactured of copper-coated FR4 composite, was employed to match a 50 Ω coaxial device (coaxial cable) to the antenna port and vice versa.[26] A microstrip exponential taper was used to combine the balun with impedance matching.[20,24] To enhance the efficiency and directivity of a dipole antenna for targeted heating, a water bolus between the radiating element (here, the SGBT building block) and the subject or phantom was used.[8,27] The water bolus was filled with deionized water (H_2O) to minimize costs; it was separated from the D_2O-filled building block with a 0.5 mm FR4 layer. The water bolus (with the dimensions 59.0 x 119.4 x 20 mm^3) was manufactured from a waterproof latex cover stabilized by a plastic ring (thickness = 5 mm).

2.2 | RF antenna building block optimization approach

The software package CST Microwave Studio 2018 (Computer Simulation Technology GmbH, Darmstadt, Germany) was used for numerical electromagnetic field (EMF) simulations and optimization. Interactions between the components of the RF antenna building block were evaluated step-by-step: (i) submerging the antenna in distilled water, (ii) placing the antenna within the building block housing with the water bolus installed, and (iii) combining the SGBT building block with the exponential stripline balun. The complex interaction of the components of the antenna design required evaluation and optimization of the geometry of the combined setup, whereas the optimization parameter space is multidimensional and listed in Table 1, including upper and lower limits as well as the optimization result. A genetic optimization algorithm implemented in CST was applied for the multidimensional optimization.[28] The population of the algorithm was set to 4 x 8 at a mutation rate of 60% with a maximum number of iterations of 60. The cost function used a reflection coefficient S_{11} ≤ -13 dB for 260 to 600 MHz and S_{11} ≤ -10 dB for 600 to 700 MHz with the objective to enable fluorine imaging (f_{19F} = 279.6 MHz), proton imaging (f_{1H} = 297.2 MHz) and MR thermometry at 7.0 T, as well as supporting a broadband frequency regime for thermal interventions. For the optimization process, a rectangular box (length = 240 mm, width = 240 mm, height = 150 mm) filled with muscle tissue mimicking material was used. For this purpose the dispersive material specifications were provided by the IT'IS Foundation (Zurich, Switzerland) for a broad frequency range.[29] This setup was used instead of an upper thigh of the virtual population to limit the computational effort.[30] The basic feasibility of a high-density array of SGBT antenna building blocks was evaluated and confirmed in EMF simulations and measurements of the nearest neighbor coupling. To cover all possible arrangements in an array configuration, the coupling (S_{21}) of the reference antenna (Ref) to the antennas A, B, and C was exemplarily investigated.

2.3 | EMF, SAR and temperature simulations

Evaluation simulations of dielectric losses, transmit RF B_1^+ field, SAR distribution and temperature were performed with the time domain solver of CST Microwave Studio 2018. Dielectric losses were analyzed for the individual components (balun, antenna, building block and water bolus) of the proposed SGBT building block. The B_1^+ efficiency was calculated by dividing the transmit RF field by the square root of the input power. Simulations were performed for a phantom validation setup (length = 210 mm, width = 140 mm, depth = 64 mm, shown in Figure 1) and for the human voxel models Ella and Duke from the virtual population using a voxel resolution of 1.0 x 1.0 x 1.0 mm^3.[30] For the simulations, the SGBT building block and the water bolus were positioned (i) in the center of the phantom surface (Figure 1D) and (ii) at the surface above the center region of the left thigh of the human voxel models. The boundary region distance between the SGBT building block filling and the water bolus was considered as 0.5 mm FR4; the water bolus latex cover was found to be ≥0.02 mm and was neglected in the simulations. The measured dielectric parameters of the phantom (based on an open-end coaxial probe setup)[31] and the tissue specifications[29] for the human voxel models were defined as dispersive to support the broadband intervention (Figure 1E). The mesh resolution was kept at ≤4.0 x 4.0 x 4.0 mm^3 for both phantom and voxel model studies. The evaluation differentiates between two modes: (i) the imaging mode at f_{19F} = 279.6 MHz and f_{1H} = 297.2 MHz, and (ii) the thermal intervention mode at f_1 = 300 MHz, f_2 = 400 MHz and f_3 = 500 MHz. For the imaging mode, both B_1^+ efficiency distribution and SAR distribution according to IEC 62704-1 standards were examined.[32] SAR was normalized to 1 W input power and averaged over 10 g of tissue (SAR_{10g}). Evaluation of the B_1^+ efficiency and SAR_{10g} distribution were assessed for a

TABLE 1 Metrics, including boundaries used and results obtained for the genetic optimization of the SGBT building block and the exponential stripline balun. The building block dimensions were considered without the housing (3 mm thickness manufactured, 0.5 mm FR4 substrate). The overall antenna length (l_{total} = 46.3 mm) is defined with the radius of the antenna bending radius (r = 7.5 mm). The building block length top ($l_{building\ block}$ = 85.1 mm) is defined with the building block scaling factor and the building block width top

Description	Lower limit	Upper limit	Optimization result
Antenna aperture angle, [°]	65	100	74
Antenna length backplane [mm]	25.0	35.0	31.3
Antenna width backplane [mm]	27.0	45.0	42.3
Antenna pin width [mm]	1.5	3.0	1.7
Balun antenna connector [mm]	1.5	6.0	4.5
Balun width [mm]	30.0	55.0	39.3
Building block width top [mm]	40.0	60.0	56.9
Building block length bottom [mm]	70.0	110.0	108.4
Building block height [mm]	12.0	30.0	18.9
Building block scale factor	1.01	1.60	1.49

central transversal slice through the left thigh of Ella and Duke. Temperature simulations were performed with a uni-directional, thermal transient solver in CST Microwave Studio's postprocessing routine. For this purpose, material parameter estimations used for the thermal intervention were derived from the literature, including phantom density (1230.89 g/l), heat capacity (2.9635 J/g/K) and thermal conductivity (0.4355 W/m/K).[33,34]

2.4 | Hardware

Bench measurements of the reflection coefficient were performed using an eight-channel vector network analyzer (VT 8, Rohde & Schwarz, Memmingen, Germany) and analyzed in MATLAB (MathWorks, Natick, MA). ^{1}H MRI, ^{19}F MRI and MR thermometry were conducted using a 7.0 T whole-body MRI system (MAGNETOM, Siemens Healthineers, Erlangen, Germany) equipped with an 8 x 1 kW RF amplifier (Stolberg HF-Technik AG, Stolberg-Vicht, Germany) and a gradient system with a maximum slew rate of 170 mT/m/ms and gradient strength of 38 mT/m (Siemens Healthineers). The heating regime setup consisted of an external signal generator (SMGL, Rohde & Schwarz) and a custom-made power amplifier supporting continuous 100 W forward power at the desired frequencies of f_1 = 300 MHz, f_2 = 400 MHz and f_3 = 500 MHz.

2.5 | Validation of EMF and temperature simulations

EMF and temperature simulations were validated using a custom-made phantom (Figure 1C-E) filled with deionized water, sucrose (994.0 g/l), NaCl (38.8 g/l), agarose (20.0 g/l) and $CuSO_4$ (0.75 g/l). Three vertically aligned polytetrafluorethylene (PTFE) plastic tubes (inner diameter = 2 mm) were placed at increasing depths in the center of the phantom to accommodate fiberoptic probes (Omniflex, Neoptix, Québec, Canada) for temperature measurements.

The performance of the developed RF antenna building block and its reflection coefficient was validated for the phantom and a healthy male human subject (aged 29 years). For transmit RF field validation, B_1^+ mapping was conducted in the phantom using 3D actual flip angle-imaging (AFI) (spatial resolution = 1.0 x 1.0 x 5.0 mm^3, TE = 2.07 ms, TR_1 = 35 ms, TR_2 = 115 ms, nominal FA = 30°, scan time = 2.25 minutes per slice, 96 slices).[35] The deviation of the measured B_1^+ field from the loss-corrected simulated B_1^+ efficiency field was calculated for the central transversal slice through the phantom. A comparison with the simulations of the B_1^+ efficiency field along three vertical lines in the transversal slice was conducted for the central, 10 mm left and 10 mm right lines. Temperature simulations were validated in a phantom study by performing heating experiments at frequencies f_1, f_2 and f_3 in conjunction with MR thermometry at 7.0 T. The antenna was connected to an external RF power amplifier (RFPA) for the heating experiments and manually reconnected to the MRI signal chain for thermometry. RF heating was performed in the iso-center of the MRI bore at room temperature (~ 297 K) for 120 seconds continuously applying P_{in} = 100 W at the antenna building block. Cable losses of <-1.9 dB were compensated for by adjusting the output amplitude of the RF power amplifier at all examined frequencies. 2D MR thermometry was conducted using the proton resonance frequency shift (PRFS) method by applying a dual gradient-echo method (spatial resolution = 1.5 x 1.5 x 4.0 mm^3, TE_1 = 2.26 ms, TE_2 = 6.34 ms, TR = 102 ms, scan time = 0.44 minutes) before and after the RF heating period.[36-39] The relative temperature mapping of PRFS after the heating process was compared with fiberoptic probe measurements.

2.6 | Ethics statement

For the in vivo feasibility study, a subject without any known history of disease was included after approval by the local ethical committee (registration number DE/CA73/5550/09, Landesamt für Arbeitsschutz, Gesundheitsschutz und technische Sicherheit, Berlin, Germany). Informed written consent was obtained from the volunteer prior to the study.

2.7 | ^{1}H and ^{19}F MR imaging

Phantom and in vivo studies were performed to demonstrate the ^{19}F and ^{1}H imaging characteristics of the SGBT building block. The tubes within the phantom, previously used for temperature measurements, were filled with high fluorine content nanoparticles prepared according to the literature.[40] ^{19}F-rich nanoparticles were prepared by emulsifying perfluoro-15-crown-5-ether (1200 mmol/L) (PFCE; Fluorochem, Hadfield, UK) with Pluronic F-68 (Sigma-Aldrich).[40] For the in vivo study, 15 g of flufenamic acid (101 mmol/L), a nonsteroidal antiinflammatory drug containing ^{19}F (Mobilat, Stada, Bad Vilbel, Germany) was sealed in a latex bag and placed on the forearm or the upper thigh of a healthy male volunteer.[10] The imaging protocol (one sagittal and three transversal slices) included:

- Phantom ^{1}H: FLASH, spatial resolution = 0.5 x 0.5 x 2.5 mm^3, TR = 50 ms, TE = 2.86 ms, nominal FA = 40°, receiver bandwidth = 260 Hz/Px, scan time = 1.18 minutes;
- Phantom ^{19}F: RARE, spatial resolution = 0.5 x 0.5 x 5.0 mm^3, TR = 1000 ms, TE = 5.20 ms, nominal FA = 180°, echo train length = 4, averages = 8, receiver bandwidth = 592 Hz/Px, scan time = 12.51 minutes;
- Forearm ^{1}H: FLASH, spatial resolution = 0.5 x 0.5 x 2.5 mm^3, TR = 90 ms, TE = 3.86 ms, nominal FA = 30°, receiver bandwidth = 260 Hz/Px, scan time = 1.18 minutes;
- Forearm ^{19}F: RARE, spatial resolution = 1.5 x 1.5 x 5.0 mm^3, TR = 2360 ms, TE = 5.60 ms, nominal FA = 180°, echo train length = 16, averages = 8, receiver bandwidth = 337 Hz/Px, scan time = 2.27 minutes;
- Thigh ^{1}H: FLASH, spatial resolution = 0.5 x 0.5 x 2.5 mm^3, TR = 90 ms, TE = 3.86 ms, nominal FA = 30°, receiver bandwidth = 260 Hz/Px, scan time = 2.20 minutes;
- Thigh^{19}F: RARE, spatial resolution = 1.5 x 1.5 x 5.0 mm^3, TR = 2000 ms, TE = 5.60 ms, nominal FA = 180°, echo train length = 16, averages = 8, receiver bandwidth = 337 Hz/Px, scan time = 2.12 minutes.

3 | RESULTS

3.1 | Characterization of the RF antenna building block

Figure 1 shows the building block with an SGBT antenna and a stripline balun after the optimization process. The weight of the filled building block was m = 150 g, with dimensions of 114.4 x 54.0 x 22.5 mm^3.

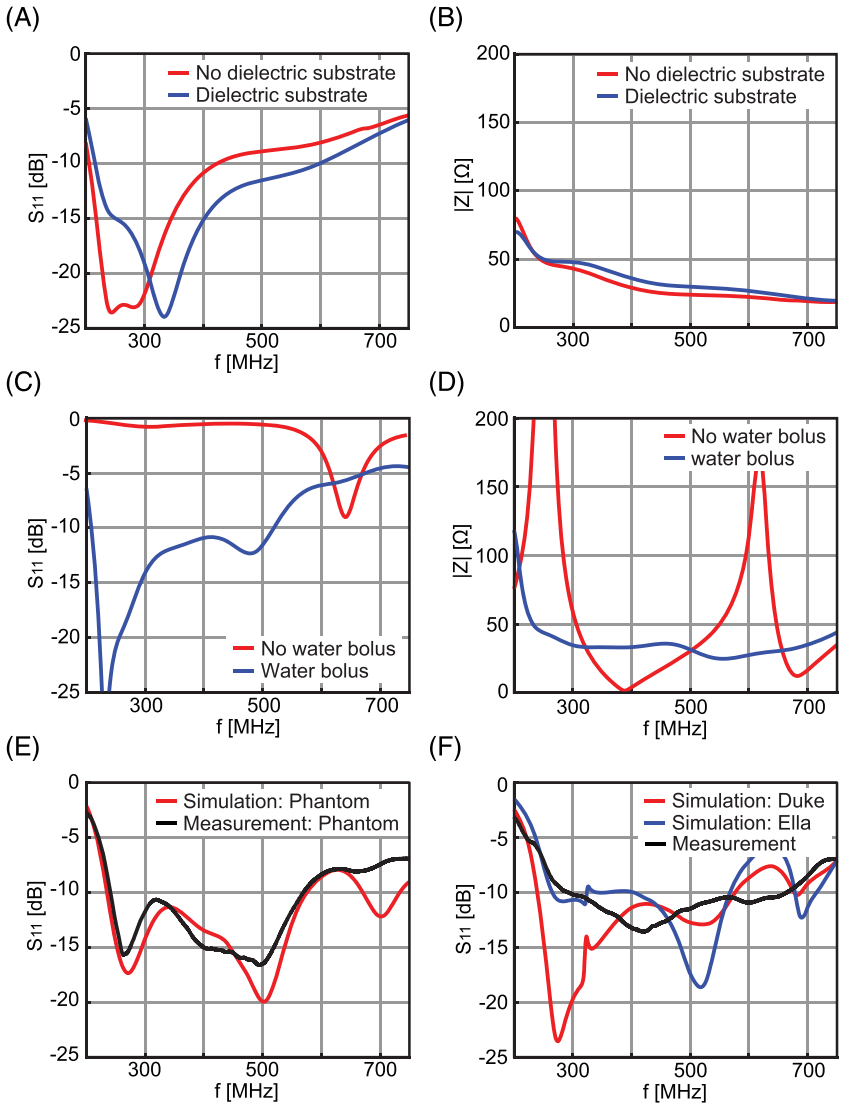

FIGURE 2 (A) Reflection coefficient (S_{11}) and (B) input impedance (Z_{11}) simulation results for the optimized antenna design immersed in distilled water with and without the dielectric layer at the tip area of the antenna. (C) S_{11} and (D) Z_{11} simulation results for the antenna within the optimized building block with and without the water bolus. (E) S_{11} simulation and measurement results of the building block antenna with balun design for the experimental setup. (F) S_{11} simulation results of the thigh of the human voxel model Duke and Ella, and experimental measurement of a healthy volunteer

EMF simulations of the individual components revealed the contributions of the RF antenna, building block, water bolus and balun to the broadband characteristics of the proposed RF antenna building block. The reflection coefficient of the antenna immersed in water showed broadband behavior with a resonance at 335 MHz. The bandwidth was increased using a low dielectric material at the tip area (Figure 2A).[19] With the dielectric material, the antenna impedance decreased from 50.6 Ω – j 19.3 Ω at 234 MHz to 28.5 Ω + j 0.8 Ω at 560 MHz (Figure 2B). The water bolus between the subject and the RF antenna building block ensured EMF propagation at a broadband frequency range (Figure 2C,D). The bolus resulted in more wideband behavior of the reflection coefficient, and a more constant impedance (49.8 Ω – j 3.9 Ω at 234 MHz to 21.4 Ω + j 14.5 Ω at 560 MHz) at the antenna feed for the SGBT building block (Figure 2C,D). Introducing the balun allowed matching of a 50 Ω coaxial cable to the 43.5 Ω differential antenna port (stripline width = 4.5 mm). The combination of the RF antenna building block with the balun resulted in an overall bandwidth of 340 MHz (for S_{11} <-10dB, f = 235 to 575 MHz).

The simulated S_{11} parameters in the phantom were in good agreement with the measured values from 250 to 650 MHz (Figure 2E). The measured cut-off frequency was increased by 6 MHz compared with the simulation, with an overall linear difference between simulation and measurement of 3.3% ± 1.9% (mean ± SD). The reflection coefficient obtained from simulations with the RF antenna building block placed on the left thigh of the human voxel model Duke and Ella exhibited a bandwidth of Δf = 337 MHz for Duke and Δf = 303 MHz with an increased minimum of S_{11} <-9.4 dB for Ella (Figure 2F). The measurement of the healthy subject provided a broadband response with an enhanced overall bandwidth ranging from 292 to 664 MHz for S_{11} <-10 dB.

Simulation and measurement of the nearest neighbor coupling between individual SGBT building blocks revealed exemplary S_{ij} <-17 dB for possible antenna arrangements in an array configuration (Figure 3).

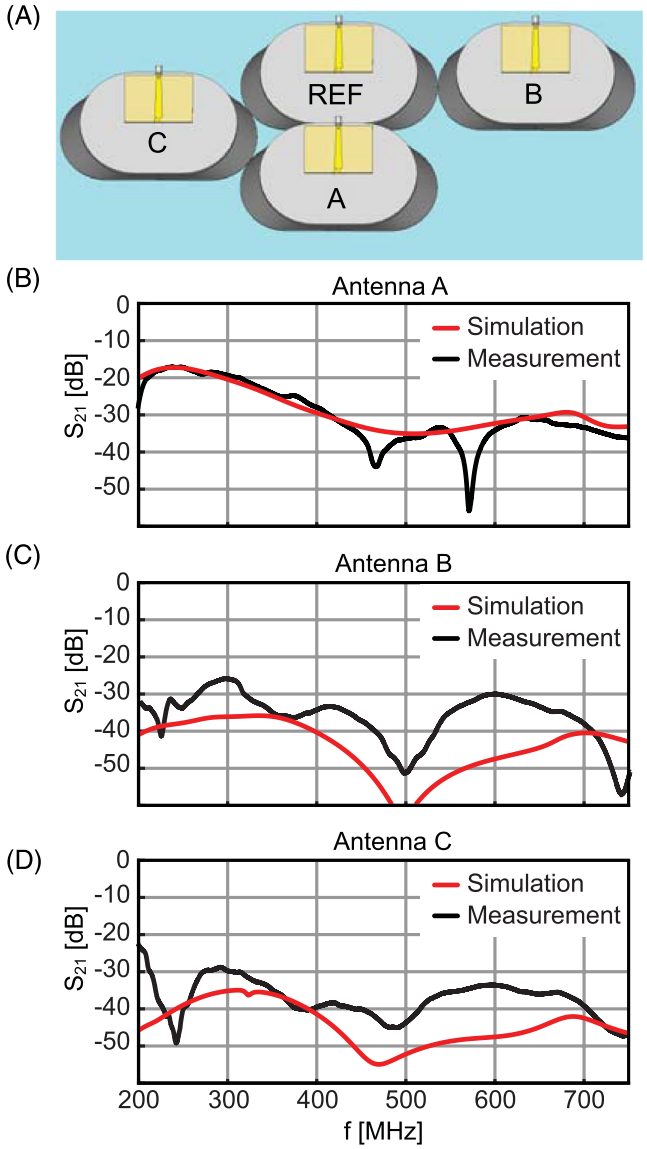

FIGURE 3 (A) Experimental setup used for the exemplary assessment of nearest-neighbor coupling of the SGBT building block. Simulated and measured coupling parameter (S_{21}) of the reference antenna (REF) to (B) antenna A, (C) antenna B and (D) antenna C

3.2 | EMF, SAR and temperature simulations

The dielectric power losses of the RF antenna building block and the water bolus ranged from 8.8% at 300 MHz to 15.6% at 500 MHz for the accepted RF power at the coaxial cable connector. The major part of the losses was due to the filled building block (5.2% at 300 MHz to 8.4% at 500 MHz) and the water bolus (2.5% at 300 MHz to 5.3% at 500 MHz). Losses for the SGBT antenna were ≤0.5%, whereas the balun showed losses of ≤1.4% for ≤500 MHz. B_1^+ efficiency maps and SAR distributions for ^{19}F and ^{1}H obtained for the human voxel models are illustrated in Figure 4. Ella showed a minor decrease in the transmission field efficiency compared with Duke. For Duke and Ella, a B_1^+ efficiency ≥11.8 μT/√kW was achieved at a depth of 50 mm (Figure 4A,B). The 1 W-normalized SAR_{10g} distribution at f_{19F} = 279.6 MHz and f_{1H} = 297.2 MHz showed a maximum SAR_{10g} = 1.8 W/kg for Ella and SAR_{10g} = 3.0 W/kg for Duke (Figure 4C,D). Considering the measured hardware losses of -3.2 dB for the RF imaging signal chain, the input power was limited to 7.0 W, to stay within the 10 W/kg for SAR_{10g} limits of the IEC guidelines for the normal operating mode.[41] The simulations on the phantom revealed a B_1^+ efficiency of ≥11.1 μT/√kW at a depth of 50 mm (Figure 5).

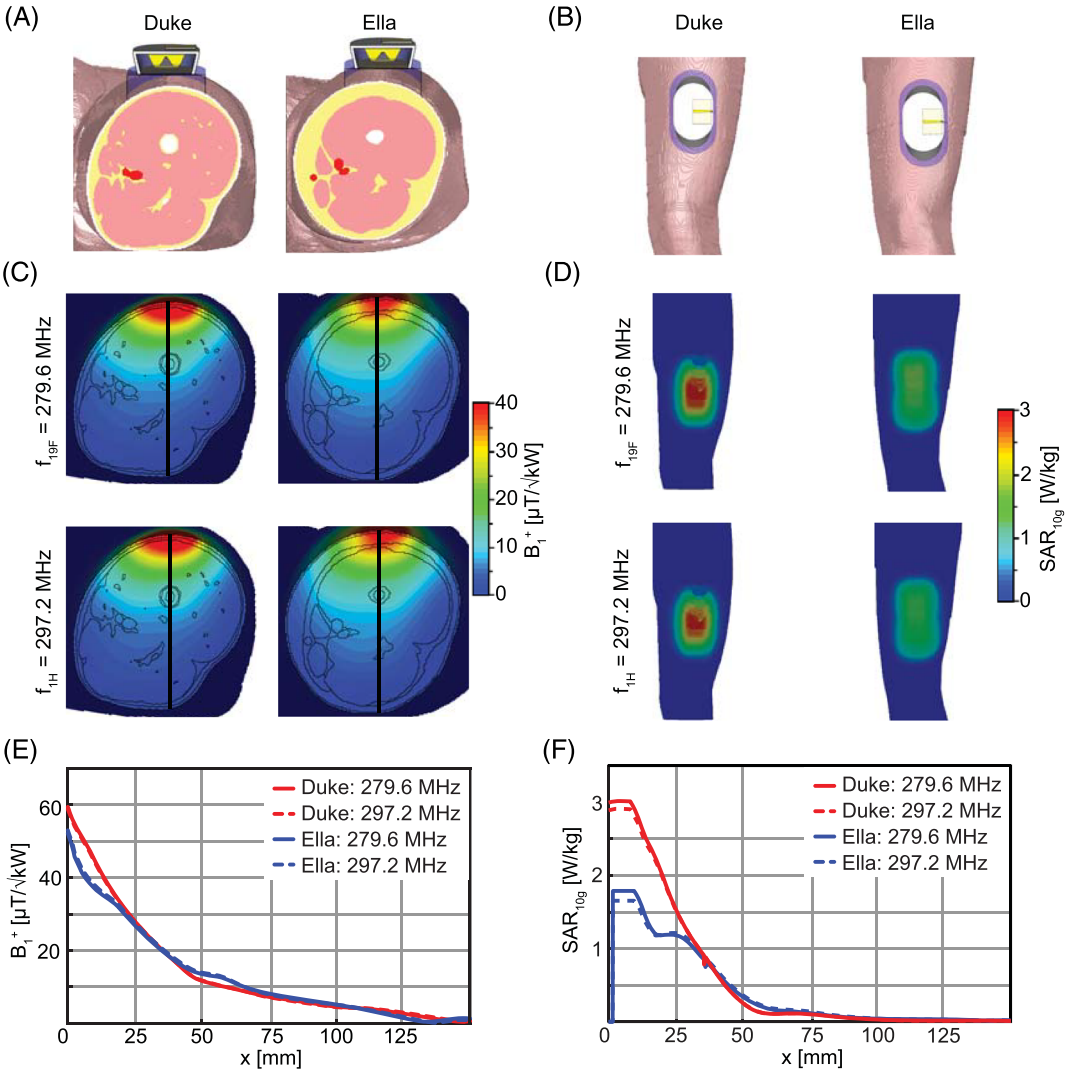

FIGURE 4 Experimental arrangement of the building block and the water bolus placed on the left thigh of the human voxel model Duke and Ella: (A) cut plane in z-direction and (B) top view. (C) Radiofrequency transmission (B_1^+) field simulation maps of the left thigh of the human voxel models for fluorine (^{19}F) and proton (^{1}H). (D) Specific absorption rate (SAR) averaged over 10 g tissue (SAR_{10g}) at f_{19F} = 279.6 MHz and f_{1H} = 297.2 MHz of the left thigh of the human voxel models. (E) Comparison of the B_1^+ field along the center line (marked in (C)) derived from the EMF simulations of the thigh of Duke and Ella. (F) Comparison of the SAR_{10g} distribution along the indicated center line (marked in (C)) of the thigh of Duke and Ella

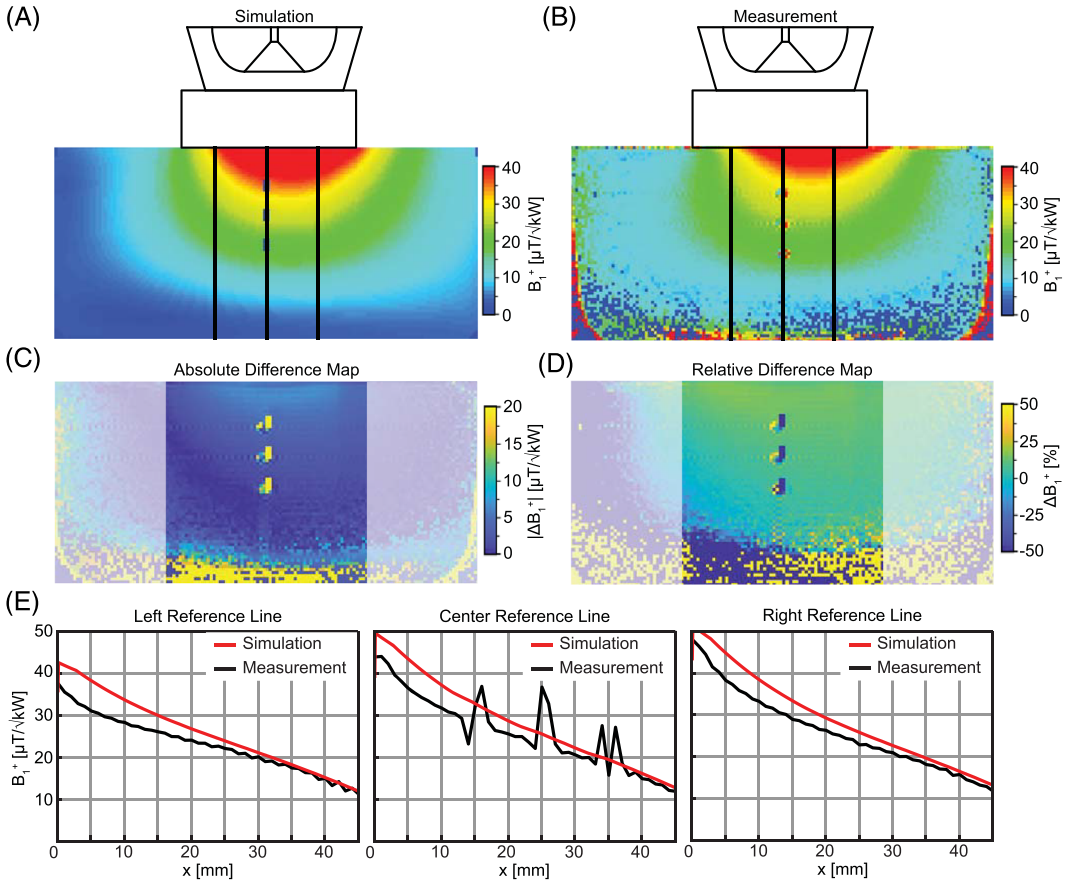

FIGURE 5 Radiofrequency transmission (B_1^+) efficiency map obtained from (A) numerical simulations and (B) experiments based on the actual flip angle imaging technique (AFI) of the indicated SGBT building block with the water bolus on the phantom. (C) Absolute and (D) relative difference maps of the simulation and the measurement of the phantom setup. (E) B_1^+ field values obtained from simulations and measurements along the lines (marked in (A) and (B)) in the phantom

Temperature simulations demonstrated the wideband thermal intervention feasibility providing a comparable heating pattern in the phantom at f_1 = 300 MHz, f_2 = 400 MHz and f_3 = 500 MHz (Figure 6).

3.3 | Validation of EMF and temperature simulations

The simulated B_1^+ efficiency maps showed qualitative and quantitative agreement with the results derived from experimental B_1^+ mapping. The difference map revealed a deviation of less than 6.7 µT/√kW (or 17%) for the central area underneath the RF antenna building block by considering the measured -3.2 dB losses in the RF signal chain. The B_1^+ profiles along the lines indicated in Figure 5A,B demonstrate both the quantitative and qualitative agreement between the simulation and the measurement.

Connecting the SGBT building block to the MRI RF signal chain employed for imaging experiments and MR thermometry took $t_{maximum}$ = 1.15 minutes. A relative difference map between simulation and MR thermometry temperature distribution and a profile along the central axis underneath the antenna, including the fiberoptic probes, is shown in Figure 6C,D. The difference between the temperature simulations and MR thermometry along the indicated vertical lines of Figure 6A,B is 0.79 ± 0.36 K for f_1, 0.82 ± 0.36 K for f_2 and 1.19 ± 0.38 K for f_3 (mean ± SD). An overall difference between simulation and measurement of 0.94 ± 0.40 K (mean ± SD) for all profiles in the performed thermal interventions was calculated. The mean difference between the fiberoptic probe measurements and MR thermometry was 0.66 K for all probe locations (Figure 6D). Probe position 1 showed a higher relative deviation (>15.4%) compared with the other measurement points (<9.3%) for all intervention frequencies (Figure 6D).

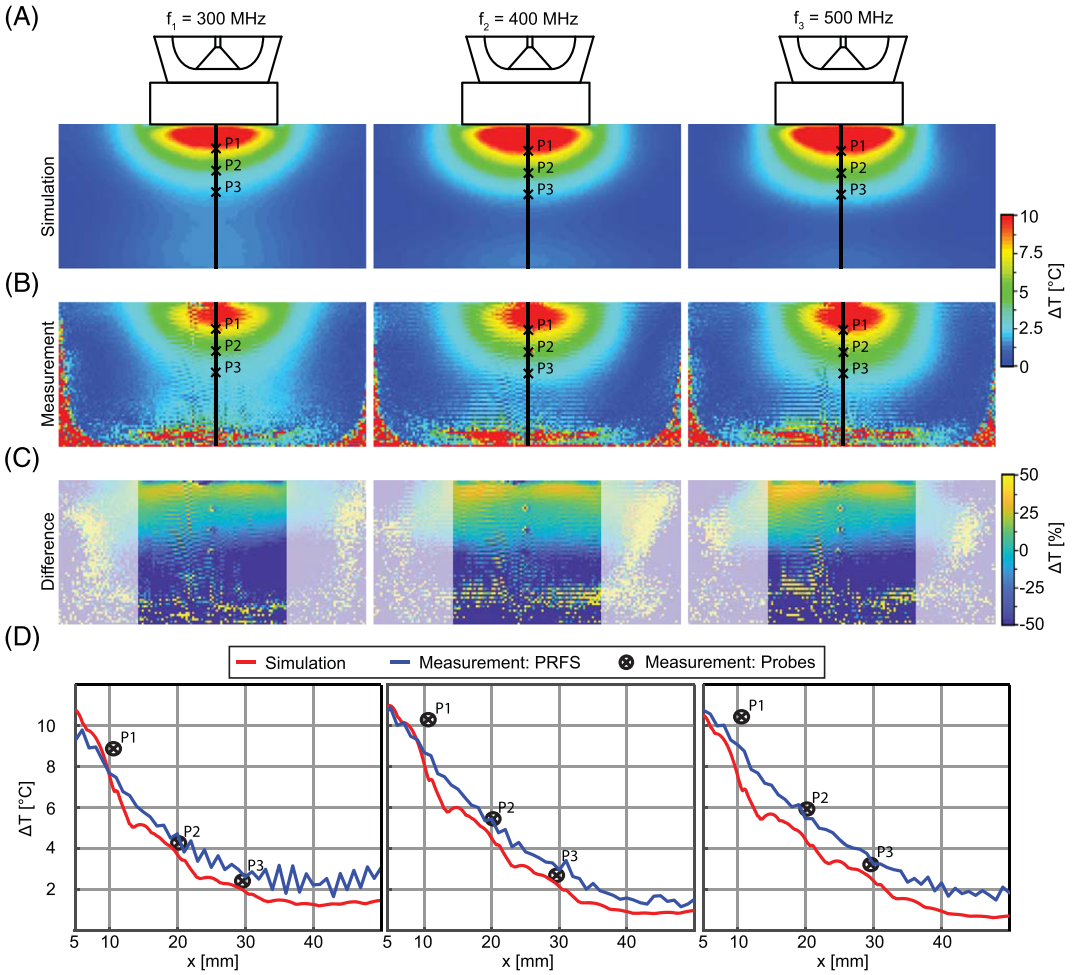

FIGURE 6 (A) Temperature simulations in the phantom after 120 seconds of thermal intervention at continuous P_{in} = 100 W at the antenna port for f_1 = 300 MHz, f_2 = 400 MHz and f_3 = 500 MHz. Highlighted are the reference line and three fibreoptic probe positions (P1-P3) used for one-dimensional plots. (B) Temperature measurements were obtained with MR thermometry based on proton resonance frequency shift (PRFS). The reference line and three fiberoptic probe positions (P1-P3) used for one-dimensional plots are highlighted. (C) Difference maps obtained from the numerical simulations and measurements of the phantom setup. (D) Comparison of the RF heating-induced temperature changes obtained from temperature simulations and experimental measurements

3.4 | ^{1}H and ^{19}F MR imaging

Imaging PFCE in the phantom study, as well as the fluorinated topical drug in the in vivo studies, showed sufficient signal to locate the compounds in the proton reference images. This demonstrates the feasibility of ^{19}F and ^{1}H imaging with the proposed broadband SGBT antenna building block without additional tuning and matching circuits (Figure 7).

4 | DISCUSSION

This work demonstrates the design and optimization of a novel wideband SGBT building block to support thermal intervention, ^{1}H MRI, ^{1}H MR temperature mapping and ^{19}F MRI integrated in a whole-body 7.0 T MRI system.

The water bolus has a significant role in the overall SGBT building block behavior; it ensures proper coupling between the building block and the object under investigation, allowing impedance matching, and forming a short waveguide-like element. This promotes the performance by (i) affording a compact size of the antenna building block, (ii) enhancing EMF coupling to the subject, and (iii) enabling broadband characteristics of the antenna. Additionally, flowing water within the bolus could be used to allow for superficial cooling during thermal interventions.[8,19,27,42] Without proper impedance matching by the water bolus, the reflection coefficient showed a single self-resonance at ~ 645 MHz. With the water bolus installed, the SGBT antenna design and the building block optimization yielded a nearly constant impedance and low-reflection coefficient for a wide bandwidth. Adapting the exponential stripline balun to the impedance at the feeding pins of the antenna allows a connection to a 50 Ω

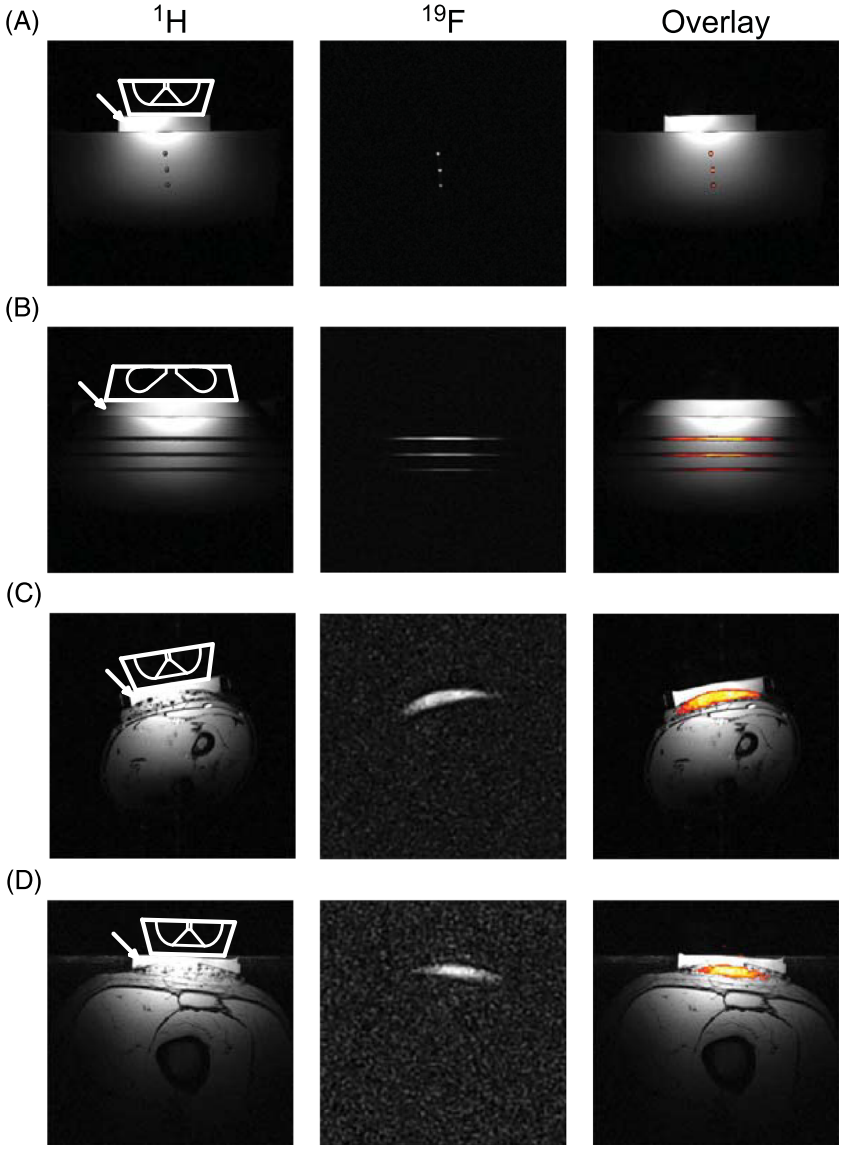

FIGURE 7 Proton image (^{1}H), fluorine image (^{19}F) and ^{19}F/^{1}H overlay. The position of the RF building block is outlined in white; the water bolus is indicated by an arrow in the ^{1}H images. Illustrated are (A phantom axial slice, (B) phantom sagittal slice, (C) forearm axial slice and (D) thigh axial slice

coaxial cable. This low-loss stripline balun is advantageous for high-peak and average-power applications such as MR imaging and thermal interventions.

The proposed compact SGBT building block affords a size reduction of 55% and 72% compared with previously reported SGBT (107 x 78 x 31 mm^3) and bow-tie (150 x 70 x 40 mm^3) RF antenna building block configurations, respectively.[18,22] A previous implementation of a single-side adapted dipole antenna that used high dielectric material to shorten the wavelength had a volume of 143 x 70 x 42 mm^3; our proposed design is 72% smaller in volume than this.[17] The size reduction is even more pronounced when benchmarking the proposed SGBT building block against pioneering dipole designs without a dielectric cavity, such as fractionated dipole (l = 300 mm),[43] snake dipole[44] or meander dipole (l = 320 mm) designs.[45] For example, a well-established implementation of the fractionated dipole uses a housing with a size of ~ 300 x 40 x 20 mm^3; our compact SGBT configuration results in a volume reduction of 52% compared with this, and a reduction in the antenna length of nearly a factor of three.[43] The compact size of the RF antenna building block and its low nearest neighbor coupling is suitable for high-density and many-element RF array configurations, which is crucial for improving the focal point quality of thermal interventions and for approaching the ultimate SAR amplification factors predicted by numerical simulations.[12-14]

The proposed antenna design shows an efficiency of 91.2% at 300 MHz and 84.4% at 500 MHz, with the dielectric losses being mainly attributed to the filled building block and the water bolus. The efficiency of the proposed building block could be increased using dedicated low-loss, high-permittivity dielectrics (eg, ceramics) close to the copper part of the SGBT antenna. The compact SGBT building block supports imaging at 7.0 T with a B_1^+ efficiency of ≥11.8 μT/√kW at a depth of 50 mm for ^{1}H and ^{19}F MRI. Although the coupling of the electric field from the building block to the subject increases due to the water bolus, the superficial SAR is still comparable with other array antenna designs by scaling the results to 1 W input power per channel.[17,43] Incorporating ^{19}F MRI adds additional value to the thermal intervention by providing the

capacity for detection and quantification of fluorinated compounds, allowing research and implementation on fluorinated, thermally activated drugs (eg, release of fluorinated compounds from thermosensitive carriers).[10,46,47] Further to ^{19}F and ^{1}H imaging, the SGBT antenna building block supports RF-induced heating for a broad frequency range. Arranged in an RF array, this feature facilitates the adjustment of the thermal intervention frequency, providing an extra degree of freedom to the thermal intervention.[12,14,19] The proton-based MR thermometry has the potential to acquire three-dimensional temperature maps, enabling a feedback loop to control RF power deposition during a thermal intervention.[48] Our temperature simulations, MR thermometry and temperature measurements showed good agreement with a temperature rise of ΔT >7 K at a depth of 10 mm. It is a recognized limitation of our proof-of-principle study that manual switching was used to change between the RFPAs used for thermal intervention and for MRI. Due to a time delay between RF heating and MR thermometry, an underestimation of the monitored temperature could occur. For clinical implementation with multiple antennas, a controllable switch is beneficial to avoid time delays and connection errors for sequential RF heating and MR thermometry.

Phantom and in vivo imaging experiments demonstrated the feasibility of a broadband RF antenna concept for ^{1}H and ^{19}F imaging without tuning and matching based on discrete inductive and capacitive elements. For ^{19}F in vivo imaging, the 15 g of topical ointment used in the proof-of-principle study showed sufficient SNR to visualize and register the ^{19}F image with the ^{1}H image. Analytically, this mass of the substance has ~ 2.9 x 10^{+21} fluorine atoms. This correlates to a bolus of the antitumor drug 5-fluorouracil administered intravenously (3.3 x 10^{+21} fluorine atoms), which afterward distributes via the blood circulation.[49] In the serum, 5-fluorouracil is present at a concentration of 1.1 and 5.9 μg/mL in the center of a tumor.[50] In the tumor, this results in a local level of 2.7 x 10^{+19} fluorine atoms/L, which is four orders of magnitude below the administered bolus concentration. Such differences in the total numbers of fluorine atoms can be addressed by increased averaging, using reduced matrix size, lower SNR thresholds and optimized scan parameters.

The broadband characteristics of the RF antenna building block are well suited for thermal interventions, since the presented RF antenna building block is less sensitive to loading conditions based on (i) a temperature increase and impedance change of the dielectric building block due to losses during the high (average) power transmission, (ii) a temperature-dependent impedance change of the water bolus or target tissue, (iii) patient movement, and (iv) intersubject variability. The balun design shows a weak suppression of common mode on the cable, which could lead to artifacts in the acquired images or crosstalk in an array configuration. A narrowband cable-trap or bazooka balun can be used to minimize the common-mode effects for MRI, where the broadband behavior is not affected. Arranging the stripline balun and the cable connector orthogonal to the electric field allowed minimization of the common-mode effects for the supported frequency bandwidth without using a blocking circuit. Whereas no signal was observed for the SGBT building block (filled with D_2O), deuterium oxide can be used to avoid the proton signal of the water bolus (filled with H_2O).

5 | CONCLUSION

The electric and magnetic characteristics of the SGBT building block support ^{1}H and ^{19}F (MRI), broadband thermal intervention (RF hyperthermia) and therapy control (MR thermometry) in an integrated device. The compact design can be exploited for the design of high-density RF applicators, offering an increased degree of freedom based on high channel count, phase and amplitude manipulation, as well as adjustable intervention frequency for each channel.

ACKNOWLEDGEMENTS

The authors wish to thank A.J.E. Raaijmakers (Utrecht Medical Center, Utrecht, the Netherlands) for fruitful discussions and for providing the dimensions of his dipole antenna systems.

This project has received funding in part from the European Research Council (ERC) under the European Union's Horizon 2020 research and innovation program under grant agreement No 743077 (ThermalMR). H.W. and E.O. were supported by a grant from the Federal Ministry for Education and Research (KMU innovativ Medizintechnik, 3-in-1 THERAHEAT, FKZ 13GW0102A, B).

FUNDING INFORMATION

This project has received funding in part from the European Research Council (ERC) under the European Union's Horizon 2020 research and innovation program under grant agreement No 743077 (ThermalMR). H.W. and E.O. were supported by a grant from the Federal Ministry for Education and Research (KMU innovativ Medizintechnik, 3-in-1 THERAHEAT, FKZ 13GW0102A, B).

ORCID

Thomas Wilhelm Eigentler https://orcid.org/0000-0001-8252-450X
Haopeng Han https://orcid.org/0000-0003-1205-2900
Andre Kuehne https://orcid.org/0000-0002-4133-5056
Helmar Waiczies https://orcid.org/0000-0001-6651-4790

Laura Boehmert https://orcid.org/0000-0002-8703-3133
Christian Prinz https://orcid.org/0000-0003-3330-031X
Hana Dobsicek Trefna https://orcid.org/0000-0001-6025-0819
Thoralf Niendorf https://orcid.org/0000-0001-7584-6527

REFERENCES

1. Datta NR, Ordóñez SG, Gaipl US, et al. Local hyperthermia combined with radiotherapy and-/or chemotherapy: Recent advances and promises for the future. *Cancer Treat Rev.* 2015;41:742-753.
2. Hooper VD. Accuracy of noninvasive core temperature measurement in acutely ill adults: the Ssate of the science. *Biol Res Nurs.* 2006;8:24-34.
3. van Rhoon GC, Wust P. Introduction: Non-invasive thermometry for thermotherapy. *Int J Hyperth.* 2005;21:489-495.
4. Titsworth WL, Murad GJA, Hoh BL, Rahman M. Fighting fire with fire: The revival of thermotherapy for gliomas. *Anticancer Res.* 2014;34:565-574.
5. Dewhirst MW, Lee C-T, Ashcraft KA. The future of biology in driving the field of hyperthermia. *Int J Hyperth.* 2016;32:4-13.
6. Lo YT, Lee SW. *Antenna Handbook: Theory, Applications, and Design*. Springer Science & Business Media; 2013. http://link.springer.com/10.1007/978-1-4615-6459-1
7. Brace C. Thermal tumor ablation in clinical use. *IEEE Pulse.* 2011;2:28-38.
8. Togni P, Rijnen Z, Numan WCM, et al. Electromagnetic redesign of the HYPERcollar applicator: toward improved deep local head-and-neck hyperthermia. *Phys Med Biol.* 2013;58:5997-6009.
9. Issels RD, Lindner LH, Verweij J, et al. Neo-adjuvant chemotherapy alone or with regional hyperthermia for localised high-risk soft-tissue sarcoma: a randomised phase 3 multicentre study. *Lancet Oncol.* 2010;11:561-570.
10. Ji Y, Waiczies H, Winter L, et al. Eight-channel transceiver RF coil array tailored for1H/19F MR of the human knee and fluorinated drugs at 7.0 T. *NMR Biomed*. 2015;28:726-737.
11. Prinz C, Delgado PR, Eigentler TW, Starke L, Niendorf T, Waiczies S. Toward 19F magnetic resonance thermometry: spin–lattice and spin–spin-relaxation times and temperature dependence of fluorinated drugs at 9.4 T. *Magn Reson Mater Phys Biol Med*. 2019;32:51-61.
12. Guérin B, Villena JF, Polimeridis AG, et al. Computation of ultimate SAR amplification factors for radiofrequency hyperthermia in non-uniform body models: impact of frequency and tumour location. *Int J Hyperth.* 2018;34:87-100.
13. Winter L, Niendorf T. Electrodynamics and radiofrequency antenna concepts for human magnetic resonance at 23.5 T (1 GHz) and beyond. *Magn Reson Mater Phys Biol Med.* 2016;29:641-656.
14. Winter L, Oezerdem C, Hoffmann W, et al. Thermal magnetic resonance: physics considerations and electromagnetic field simulations up to 23.5 Tesla (1GHz). *Radiat Oncol.* 2015;10:201.
15. Oberacker E, Kuehne A, Nadobny J, et al. Radiofrequency applicator concepts for simultaneous MR imaging and hyperthermia treatment of glioblastoma multiforme. *Curr Dir Biomed Eng.* 2017;3:473-477.
16. Raaijmakers AJE, Luijten PR, van den Berg CAT. Dipole antennas for ultrahigh-field body imaging: a comparison with loop coils. *NMR Biomed.* 2016;29:1122-1130.
17. Raaijmakers AJE, Ipek O, Klomp DWJ, et al. Design of a radiative surface coil array element at 7 T: The single-side adapted dipole antenna. *Magn Reson Med.* 2011;66:1488-1497.
18. Paulides MM, Bakker JF, Zwamborn APM, van Rhoon GC. A head and neck hyperthermia applicator: Theoretical antenna array design. *Int J Hyperth.* 2007; 23(1):59-67.
19. Takook P, Persson M, Gellermann J, Trefná HD. Compact self-grounded Bow-Tie antenna design for an UWB phased-array hyperthermia applicator. *Int J Hyperth.* 2017;33:387-400.
20. Takook P, Trefna HD, Zeng X, Fhager A, Persson M. A computational study using time reversal focusing for hyperthermia treatment planning. *Prog Electromagn Res B.* 2017;73:117-130.
21. Kok HP, Van Stam G, Bel A, Crezee J. A mixed frequency approach to optimize locoregional RF hyperthermia. 2015 European Microwave Conference (EuMC) "Freedom Through Microwaves". *EuMC.* 2015:773-776.
22. Winter L, Trefná HD, Ji Y, Huelnhagen T, Niendorf T. Ultrahighfield, One for all: Ultra-wideband (279-500MHz) self-grounded bow-tie antenna for MR, and thermal. In: *ISMRM-ESMRMB 26.* Joint Annual Meeting 2018:#4281.
23. Eigentler TW, Winter L, Han H, et al. Ultra-Wideband Self-Grounded Bow-Tie Antenna Building Block for Thermal Intervention, Diagnostic MRI and MR Thermometry at 7.0 Tesla. In: *ISMRM 27.* Annual Meeting 2019:#3827.
24. Yang J, Kishk A. A novel low-profile compact directional ultra-wideband antenna: the self-grounded bow-tie antenna. *IEEE Trans Antennas Propag.* 2012;60:1214-1220.
25. Paulides MM, Mestrom RMC, Salim G, et al. A printed Yagi–Uda antenna for application in magnetic resonance thermometry guided microwave hyperthermia applicators. *Phys Med Biol.* 2017;62:1831-1847.
26. Kazemipour A, Begaud X. Calculable dipole antenna for EMC measurements with low-loss wide-band balun from 30 MHz to 2 GHz. *Electromagnetics.* 2005;25:187-202.
27. Rijnen Z, Togni P, Roskam R, Van De Geer SG, Goossens RHM, Paulides MM. Quality and comfort in head and neck hyperthermia: A redesign according to clinical experience and simulation studies. *Int J Hyperth.* 2015;31:823-830.
28. Jones EA, Joines WT. Design of Yagi-Uda antennas using genetic algorithms. *IEEE Trans Antennas Propag.* 1997;45:1386-1392.
29. IT'IS Foundation. Tissue Properties Database V4.0. IT'IS Foundation.
30. Christ A, Kainz W, Hahn EG, et al. The virtual family - development of surface-based anatomical models of two adults and two children for dosimetric simulations. *Phys Med Biol.* 2010;55:N23-N38.
31. Athey TW, Stuchly MA, Stuchly SS. Measurement of Radio Frequency Permittivity of Biological Tissues with an Open-Ended Coaxial Line: Part I. *IEEE Trans Microw Theory Tech.* 1982;30:82-86.
32. IEC Committee. IEEE 62704-1-2017 - IEC/IEEE International Standard for Determining the Peak Spatial Average Specific Absorption Rate (SAR) in the Human Body from Wireless Communications Devices, 30 MHz - 6 GHz. Part 1: General Requirements for using the Finite Difference. 2017.

33. Asadi M. *Beet-Sugar Handbook*. John Wiley & Sons. Wiley-Interscience; 2007. https://www.wiley.com/en-us/Beet+Sugar+Handbook-p-9780471763475.
34. Buchanan EJ. Economic design and operation of process heat exchange equipment. *Proc S Afr Sug Technol Ass*. 1966;44:89-101.
35. Yarnykh VL. Actual flip-angle imaging in the pulsed steady state: A method for rapid three-dimensional mapping of the transmitted radiofrequency field. *Magn Reson Med*. 2007;57:192-200.
36. Depoorter J, Dewagter C, Dedeene Y, Thomsen C, Stahlberg F, Achten E. The proton-resonance-frequency-shift method compared with molecular diffusion for quantitative measurement of two-dimensional time-dependent temperature distribution in a phantom. *J Magn Reson Ser B*. 1994;103:234-241.
37. Bing C, Staruch RM, Tillander M, et al. Drift correction for accurate PRF-shift MR thermometry during mild hyperthermia treatments with MR-HIFU. *Int J Hyperth*. 2016;32:673-687.
38. Rieke V, Butts PK. MR thermometry. *J Magn Reson Imaging*. 2008;27:376-390.
39. Winter L, Oberacker E, Paul K, et al. Magnetic resonance thermometry: Methodology, pitfalls and practical solutions. *Int J Hyperth*. 2016;32:63-75.
40. Waiczies S, Lepore S, Sydow K, et al. Anchoring dipalmitoyl phosphoethanolamine to nanoparticles boosts cellular uptake and fluorine-19 magnetic resonance signal. *Sci Rep*. 2015;5:8427.
41. International Electrotechnical Commission. IEC 60601-2-33 Medical electrical equipment - Part 2-33: Particular requirements for the basic safety and essential performance of magnetic resonance equipment for medical diagnosis. *Int Electrotech Comm*. 2015;1-121.
42. Drizdal T, Paulides MM, van Holthe N, van Rhoon GC. Hyperthermia treatment planning guided applicator selection for sub-superficial head and neck tumors heating. *Int J Hyperth*. 2018; 34(6):704-713.
43. Raaijmakers AJE, Italiaander M, Voogt IJ, et al. The fractionated dipole antenna: A new antenna for body imaging at 7 Tesla. *Magn Reson Med*. 2016;75:1366-1374.
44. Steensma B, Viviana A, Andrade O, Klomp D, Luijten P, Raaijmakers A. Body imaging at 7 Tesla with much lower SAR levels: an introduction of the Snake Antenna array. *Proc Intl Soc Mag Reson Med*. 2016;24:0395.
45. Chen G, Cloos M, Sodickson DK, Wiggins G. A 7T 8 channel transmit-receive dipole array for head imaging: dipole element and coil evaluation. *Proc Intl Soc Mag Reson Med*. 2014;22(22):4572.
46. Langereis S, Keupp J, van Velthoven JL, et al. A temperature-sensitive liposomal 1 H CEST and 19 F contrast agent for MR image-guided drug delivery. *J Am Chem Soc*. 2009;131:1380-1381.
47. de Smet M, Langereis S, van den Bosch S, Grüll H. Temperature-sensitive liposomes for doxorubicin delivery under MRI guidance. *J Control Release*. 2010;143:120-127.
48. Ranneberg M, Weiser M, Weihrauch M, Budach V, Gellermann J, Wust P. Regularized antenna profile adaptation in online hyperthermia treatment. *Med Phys*. 2010;37:5382-5394.
49. Bécouarn YH, Brunet RC, Rouhier MLP, et al. High dose folinic acid and 5-fluorouracil bolus and continuous infusion for patients with advanced colorectal cancer. *Cancer*. 1995;76:1126-1131.
50. Zheng J-F, Wang H-D. 5-Fluorouracil concentration in blood, liver and tumor tissues and apoptosis of tumor cells after preoperative oral 5'-deoxy-5-fluorouridine in patients with hepatocellular carcinoma. *World J Gastroenterol*. 2005;11:3944-3947.

How to cite this article: Eigentler TW, Winter L, Han H, et al. Wideband Self-Grounded Bow-Tie Antenna for Thermal MR. *NMR in Biomedicine*. 2020;33:e4274. https://doi.org/10.1002/nbm.4274